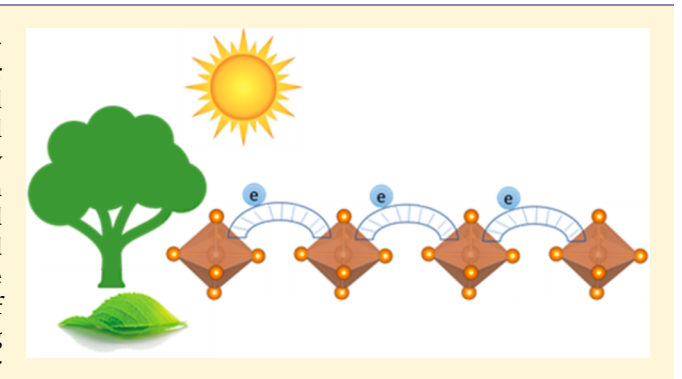


Zero-Dimensional Organic-Inorganic Perovskite Variant: Transition between Molecular and Solid Crystal

Ming-Gang Ju, † Jun Dai, † Liang Ma, † Yuanyuan Zhou, and Xiao Cheng Zeng*, † ‡

Supporting Information

ABSTRACT: Low-dimensional organic-inorganic halide perovskites (OIHPs) have attracted intense interest recently for photovoltaic applications, due to their markedly high chemical stability as compared to the widely studied three-dimensional (3D) counterparts. However, low-dimensional OIHPs usually give much lower device performance than the 3D OIHPs. In particular, for the zero-dimensional (0D) OIHPs, it is believed that the strong intrinsic quantum-confinement effects can lead to extremely low carrier motility, which can severely limit the photovoltaic performance. Herein, we predict a new family of 0D perovskite variants that, surprisingly, exhibit outstanding optoelectronic properties. We show that the "atypical" carrier



mobility of these new 0D perovskites is attributed to the strong electronic interaction between neighboring octahedrons in the crystal. These findings also suggest a new materials design strategy for resolving the low-performance issue commonly associated with the low-dimensional OIHPs for photovoltaic applications.

INTRODUCTION

Organic-inorganic halide perovskites (OIHPs) represent a major milestone in the development of high-performance materials for optoelectronic applications, for example, in photovoltaics (PVs),¹⁻⁷ light-emitting devices,⁸ and photo/ X-ray detectors. Within only several years, polycrystalline thin-film perovskite photovoltaic devices have achieved a power conversion efficiency (PCE) of 23.3%. 10 However, the large-scale application of OIHP-based solar cells is still hampered by the instability and toxicity issues associated with the prevailing OIHPs, which contain hygroscopic organic (methylammonium (MA+) or formanidium (FA+)) and lead (Pb) cations. To address both issues, much research effort has been devoted to seeking highly stable Pb-free perovskites for PVs. The most straightforward strategy is the homovalent substitution of Pb2+ with other divalent cations such as tin (Sn²⁺)¹¹⁻¹³ and/or germanium (Ge²⁺). However, previous studies showed that this strategy results in Pb-free perovskites with very poor stability due to the high chemical activity of Sn²⁺ and Ge²⁺. Other design strategies include (1) incorporation of metal cations (e.g., Sb^{3+} , 7,16 Bi^{3+} , 17 Ag^{+}) 17,18 with different valences to form perovskite derivatives with new chemical formula, such as $A_3B_2^{3+}X_9$ and $A_2B_2^{1+}B_2^{3+}X_6$ (X represents halogen element), rather than the conventional ABX₃ perovskite; ¹⁹ and (2) development of lower-dimensional structures (2D, 1D, or 0D).^{20,21} For 3D OIHPs, their crystal structures typically exhibit continuous network of cornersharing [BX₆] octahedron in all directions, whereas for low-

dimensional OIHPs, the connection of [BX₆] octahedron is discontinuous in certain directions. Among all of the lowdimensional OIHPs, 2D Ruddleson-Popper perovskites have been studied the most because high PV performance can be achieved by controlling the crystallographic anisotropy in the thin films. 22,23 Several studies on 1D perovskites, where the [BX₆] octahedron is connected along a chain, have also been reported in the literature. 24,25 Note that the low dimensionality typically results in self-trapping exciton due to strongly exciton-phonon interaction, which is undesirable for the PV applications. 21,25-27 In 0D perovskites, such exciton selftrapping is expected to be even more undesirable.²⁸ As such, it is generally viewed that 0D perovskites are unsuitable for making good PSCs. However, it has been shown that 0D perovskites based on Ti²⁹ and Sb can still exhibit outstanding optoelectronic properties, and give promising device PCE values of 3.2% and 3.8%, respectively. 30,31 Such an unexpected PCE performance calls for new theoretical insights into the unique properties of the atypical 0D perovskites, as well as has important implication to the rational design of new 0D perovskite materials for PV application.

In this Article, we report a series of 0D perovskites (variants), ABX6, where A denotes an organic or inorganic cation [e.g., Cs⁺, MA⁺, FA⁺, n-propylammonium (C₃H₉N⁺), nbutylammonium (BA⁺), pyridinium ($C_5H_6N^+$), tropylium

Received: April 12, 2018 Published: July 25, 2018



10456

[†]Department of Chemistry, and [‡]Department of Chemical & Biomolecular Engineering and Department of Mechanical & Materials Engineering, University of Nebraska-Lincoln, Lincoln, Nebraska 68588, United States

[§]School of Engineering, Brown University, Providence, Rhode Island 02912, United States

 $(C_7H_7^{+})$, and ethylpyridinium $(N\text{-EtPy}^+)$], X is a halogen anion (e.g., Br $^-$ or Cl $^-$), and B is Sb $^{5+}$, Bi $^{5+}$, and V $^{5+}$, respectively. On the basis of the theoretical computation, we predict that many 0D perovskites can possess direct and suitable bandgap for PV applications. We have also shown that the unique optoelectronic properties of the 0D perovskites are due to the structural arrangement of octahedrons in the crystal, as well as the sp hybrid orbitals contribution to the conduction band minimum (CBM).

■ RESULTS AND DISCUSSION

Figure 1A shows the crystalline structure of ABX₆ viewed from the [010] and [101] directions with distinct features of 0D perovskite compounds. Contrary to other prevailing 0D

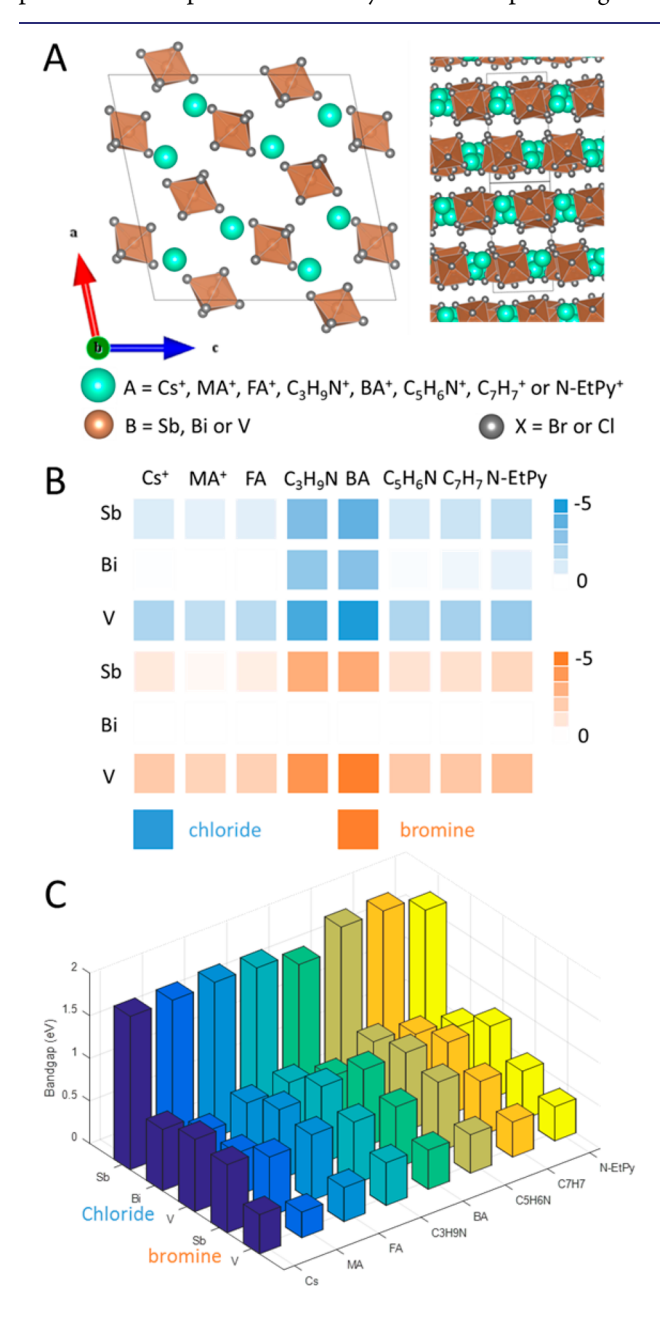


Figure 1. (A) Crystalline structures of ABX $_6$ viewed from [010] (left) and [101] (right). (B) Computed formation energies of a series of compounds ABX $_6$. (C) Computed bandgaps of a series of compounds ABX $_6$ based on PBE functional.

perovskite compounds, such as Cs_2SnI_6 or Cs_2TiBr_6 , in which vacancies and octahedrons are alternatively arranged to form vacancy-order double perovskite halide, here, viewing from the [010] direction, octahedrons $[BX_6]^{-1}$ and cations are respectively arranged into two rows, while the two rows are arranged alternatively along the [101] direction. Viewing from the [101] direction are layers, consisting of rows of octahedrons $[BX_6]^{-1}$ and cations, stacking to form lamellar structures. The distances between neighboring octahedrons $[BX_6]^{-1}$ and local configurations are very different from those of Cs_2SnI_6 and Cs_2TiI_6 . The distinct structural features of ABX_6 crystal imply new properties, not seen in other 0D perovskite compounds.

To assess the stability of the new 0D material against decomposition, we compute the formation energy corresponding to the synthetically routes often used for making ABX₆, for example, these decomposition pathways $ABX_6 = AX + X_2 +$ BX_{3} , $ABX_{6} = AX + BX_{5}$, and $ABX_{6} = ABX_{3} + (3/2)X_{2}$. Most formation energies are calculated on the basis of $ABX_6 = AX +$ $X_2 + BX_3$ except ASbCl₆ compounds, which are calculated on the basis of $ABX_6 = AX + BX_5$. Additionally, due to the lack of information on ASbX₃ and ABiX₃, we only considered ABX₆ = $ABX_3 + (3/2)X_2$ for $CsVX_6$, $MAVX_6$, and $FAVX_6$ compounds. These calculated formation energies show that this is not a favorable pathway for decomposition of these compounds with respect to other pathways. Figure 1B shows the computed formation energies of a series of ABX₆ chlorides and bromines. It can be seen that most chlorides are predicted to be thermodynamically stable. When the cations are N-EtPy⁺, BA⁺, and C₃H₉N⁺, the compounds exhibits higher stabilities. For bromines, due to the electropositivity of Bi⁵⁺, no stable configures are obtained from our calculations. Analogous to chlorides, the stability of Sb- and V-based compounds exhibit a similar trend.

Next, the electronic properties of these compounds are computed, such as the bandgaps, on the basis of the PBE functional. As shown in Figure 1C, chlorides possess wider bandgaps than those of bromines. Sb-based chlorides possess the widest bandgaps as compared to the others, while Sb-based bromines possess wider bandgaps than the V-based bromine. Bi-based chlorides possess bandgaps similar to those of Sb-based bromines. Note that the different sized cation A⁺ can significantly affect the bandgaps of compounds. With different cations, the variation of bandgaps amounts to 0.4 eV.

To gain deeper insight into the effect of different cations, we have calculated band structures and density of states (DOS) for CsSbBr₆, *N*-EtPySbBr₆, CsBiCl₆, *N*-EtPyBiCl₆, CsVBr₆, and *N*-EtPyVBr₆, respectively. As shown in Figure S1, *N*-EtPySbBr₆ exhibits more dispersive valence bands than CsSbBr₆, suggesting that *N*-EtPySbBr₆ has a higher carrier mobility, an important property required for PV application. Especially, by substituting the *N*-EtPy⁺ with Cs⁺, the distribution range of lower conduction bands extends from 0.58 to 1.0 eV, which benefits the electron mobility enhancement. Besides, the flat highest valence band of CsSbBr₆ and *N*-EtPySbBr₆ results in heavier hole effective mass, implying that both compounds are n-type semiconductor.

The computed partial density of states (PDOSs) of CsSbBr₆ and N-EtPySbBr₆ show that the valence band maximum (VBM) is mostly contributed by Br 5p orbitals, while the conduction band minimum (CBM) is contributed mostly by Br 5p orbitals and some by Sb 5s orbitals. The A-site cations, for example, Cs⁺ and N-EtPy⁺, seem not to contribute to the

bandgap edges directly, but only indirectly affect the electronic property through changing the crystalline structure. Clearly, these electronic properties are quite different from those of typical 0D compound Cs₄PbBr₆, which exhibits nearly nondispersive transport along all directions, resulting in heavy carriers (see Figure S4). The computed PDOSs of Cs₄PbBr₆ show that the VBM is contributed mostly by Br 4p orbitals and some by Pb 6s orbitals, while the CBM is contributed mostly by Pb 6p orbitals and some by Br 4p orbitals. The A-site cation Cs+ does not contribute to the band gap edges. Intuitively, the different arrangements of octahedrons [SbX₆]⁻¹ and [PbBr₆]⁻⁴ in the two 0D compounds should affect the electronic properties and result in the different band structures.

Figure S2 displays the band structures and PDOSs of CsBiCl₆ and N-EtPyBiCl₆. The N-EtPyBiCl₆ exhibits a band structure characteristic similar to that of N-EtPySbBr₆, for example, more dispersive conduction bands than CsBiCl61 whereas CsBiCl₆ exhibits more flat valence bands than N-EtPyBiCl6. The computed PDOSs show that the VBM is contributed by Cl 3p orbitals and the CBM is contributed by Cl 3p and Bi 6s orbitals. In contrast, the lower conduction bands of CsVBr₆ have more delocalized energy distribution than N-EtPyVBr₆ (see Figure S3). Like Cs₄PbBr₆, the flat lower conduction bands and higher valence bands of the two compounds indicate that both compounds have heavier carriers and features of strong quantum confinement. The computed PDOSs show that the VBM is contributed by Br 4p orbitals and the CBM is mostly contributed by V 3d and Br 4p orbitals.

To provide a better quantitative estimate for the effect of Asite cations, we computed the bandgaps of a series of ASbBr₆ using accurate hybrid DFT (HSE06 functional). As shown in Figure 2A, CsSbBr₆ has the widest bandgap of 1.85 eV as compared to the others. Note that the computed bandgaps of the MASbBr₆ and N-EtPySbBr₆ are within optimal range of 0.9-1.6 eV for PV applications. With increasing the radii of Asite cation from MA⁺ to N-EtPy⁺, there is no obvious trend for bandgap change, which is different with 3D OHIPs. This stems from that shapes of organic cations in 3D OHIPs may approximately be as spheres, whereas the shapes of cations in 0D OHIPs significantly affect the arrangement of octahedrons. Comparing the structural configuration of octahedrons [SbBr₆]⁻¹ in these compounds, it is interesting that the angle between neighboring octahedrons along a line is changed by changing the A-site cations (see inset in Figure 2B). The angle is respectively about 45° and 13°, while the bandgap is 1.9 and 1.55 eV for CsSbBr₆ and N-EtPySbBr₆, respectively. To assess the effect of angle change, we compute the bandgaps by artificially increasing the angle. As shown in Figure 2B, the bandgap slightly decreases with increasing the angle from 0° to 20° , sharply increases from 20° to 40° , and then levels off to a value. The strong effect of A-site cations promotes such a test of different inorganic and organic cations on changing the electronic properties of ASbBr₆ compounds. The N-EtPy⁺ can obviously improve the optoelectronic properties of Sb and Bi based compounds, and also can affect the electronic property of V-based compounds. Hereafter, we mainly focus on the N-EtPyBX₆ compounds, for example, N-EtPySbBr₆, N-EtPyBiCl₆, and N-EtPyVBr₆. Meanwhile, we have also performed ab initio molecular dynamic (AIMD) simulations to estimate the stabilities of these three compounds (see Figure S5). It can be seen that these 0D perovskite frameworks of these

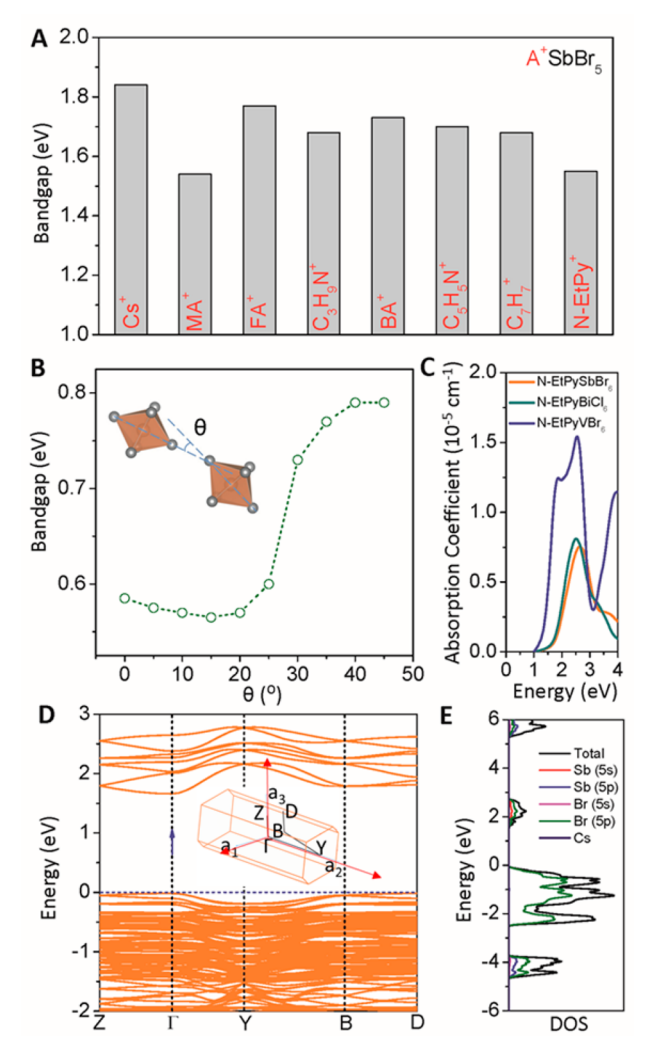


Figure 2. (A) Computed bandgaps of a series of ASbBr₆ based on the HSE06 functional. (B) Computed bandgaps (based on PBE functional) of $CsSbBr_6$ with increasing angles between neighboring octahedrons $[SbBr_6]^{-1}$. (C) Computed optical absorption spectra of N-EtPySbBr₆, N-EtPyBiCl₆, and N-EtPyVBr₆ based on PBE functional, and blueshifted by the HSE06 correction of 1.0 eV. (D) Band structure (based on HSE06 functional) of N-EtPySbBr₆. Here, Γ (0.0, 0.0, 0.0), Z (0.0, 0.0, 0.5), Y (0.0, 0.5, 0.0), B (-0.5, 0.0, 0.0), and D (-0.5, 0.0, 0.5) refer to the high-symmetry special points in the first Brillouin zone (inset is Brillouin zones of unit cells). (E) PDOSs of N-EtPySbBr₆ (based on HSE06 functional).

compounds are well sustained in the final configuration, indicating that these compounds possess good thermal stabilities.

Figure 2C displays the computed absorption spectra of three compounds. Clearly, N-EtPyVBr₆ exhibits stronger absorption in the visible-light region than do the other two compounds. N-EtPySbBr₆ and N-EtPyBiCl₆ display comparable absorption in the visible region. Although their absorption intensities are slightly lower, they still possess suitable bandgaps and reasonably good optical absorption properties. Figure 2D shows the computed band structures of N-EtPySbBr₆, based on HSE06 functional. Similar to the band structure (PBE), N-EtPySbBr₆ exhibits a direct bandgap with the VBM and CBM being located at the Γ point, a steeper lowest conduction band, and a flatter highest valence band. The latter suggests light electron carrier and heavy hole carrier. The HSE06 bandgap of 1.55 eV is much larger than the PBE bandgap of 0.56 eV. We also calculated the effective masses of the N-EtPySbBr $_6$ along the $[\overline{1}00]$, [010], and [001] directions, respectively. The electron effective masses at the Γ point are 0.72, 0.49, and 0.56 m_e , respectively, while the hole effective masses at the Γ point are -2.16, -0.85, and -3.91 m_e , respectively. Notably, the hole effective masses are much heavier than the electron effective masses, confirming the inference of carrier mobility. The projected HSE06 DOS values on the Sb 5s, Sb 5p, Br 4s, and Br 4p exhibit the same feature around bandgap edges as those based on the PBE (see Figure 2E).

Figure S6A,B shows the HSE06 band structure and DOS of N-EtPyBiCl₆, which is similar to that of N-EtPySbBr₆, because Bi and Sb, and Cl and Br belong to the same group in the periodic table, respectively. N-EtPyBiCl₆ also exhibits a direct bandgap with VBM and CBM being located at the Γ point. The HSE06 bandgap is about 1.65 eV. It is known that for the perovskites with heavy metal element, the spin-orbit coupling (SOC) can significantly reduce the bandgap. Figure S6C,D shows computed HSE06 DOSs of N-EtPyBiCl₆ with and without considering SOC. There is a negligible SOC effect on the bandgap and character of DOS near the bandgap edge. The reason may be due to that the VBM and CBM of N-EtPyBiCl₆ are mostly contributed by Cl 3p orbitals with only a minor contribution of Bi 6s orbitals to the CBM. On the other hand, the band structure of N-EtPyVBr₆ exhibits very different characters (see Figure S7A), for example, an indirect bandgap with flatter lowest conduction band, as compared to those of N-EtPySbBr₆ and N-EtPyBiCl₆. The CBM is mostly contributed by the V 3d orbital, but not by Br 4p orbitals, resulting in flat conduction bands (see Figure S7B). Figure S8 shows the charge density distributions corresponding to CBM and VBM for the three compounds. Clearly, those of VBMs that exhibit dumbbell contour of p orbitals are localized on the halide, demonstrating that the VBMs are mostly contributed by p orbital of halides. For N-EtPySbBr6 and N-EtPyBiCl6, the charge distribution corresponding to CBM is delocalized on the metal and halide. For N-EtPyVBr₆, the charge distribution corresponding to CBM is localized on V with contour of d orbital.

From the view of configuration, 0D perovskite materials resemble molecular crystals, but molecular crystals are generally composed of organic molecules (e.g., pentacene), whereas 0D perovskite materials are composed of inorganic components or hybrid inorganic/organic components (e.g., Cs₄PbBr₆ and (C₇H₇)₂SnI₆³²). Properties of molecular crystals are largely dependent on the interaction between neighboring molecules. Likewise, the properties of 0D perovskite materials with octahedrons $[BX_6]^{-1}$ are expected to be mostly dependent on the interaction between neighboring octahedrons. Yin et al. have indicated that due to the weak interaction between neighboring octahedrons, Cs₄PbBr₆ possesses electronic zero dimensionality, thereby having a low carrier mobility.²⁸ To gain insight into the relationship between the electronic properties and interaction of octahedrons for N-EtPySbBr₆, N-EtPyBiCl₆, and N-EtPyVBr₆, we compute the electronic structure and optoelectronic properties of monomer, dimer, and tetramers of octahedrons [SbBr₆]⁻¹, [BiCl₆]⁻¹, and [VBr₆]⁻¹ using the time-dependent DFT (TD-DFT) method.

Figure 3A shows configures of monomer, dimer, and tetramers in the crystal structure for our calculation. For monomer, a single $[SbB_6]^{-1}$ unit, all of the Sb–Br bond lengths are 2.59 Å (see Table S1). The computed optical

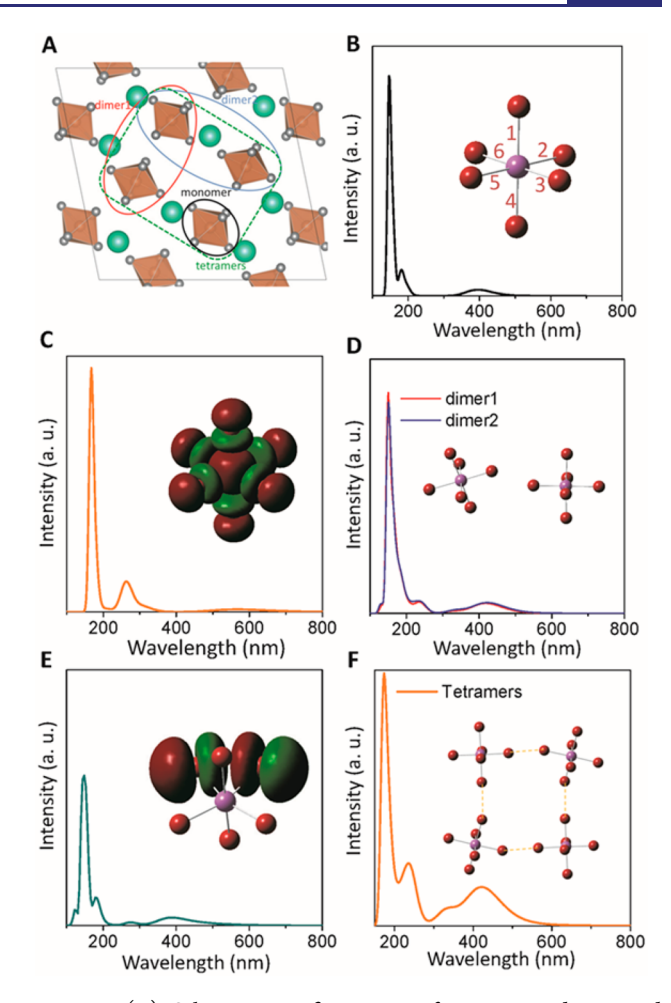


Figure 3. (A) Schematic configurations of monomer, dimer, and tetramers for $[SbBr_{\rm G}]^{-1}$. (B) Absorption spectrum of monomer with neutral state. The configuration and labels of bonds are given in the inset. (C) Absorption spectrum of monomer with negative polaron state. The spin distribution of negative polaron is given in the inset. (D) Absorption spectrum of dimers with neutral state. The configuration of dimer is given in the inset. (E) Absorption spectrum of monomer with positive polaron state. The spin distribution of positive polaron is given in the inset. (F) Absorption spectrum of tetramers with neutral state. The configuration of tetramers is given in the inset.

absorption spectrum of monomer is displayed in Figure 3B. There is a weak absorption peak at 400 nm wavelength, and a main absorption peak below 200 nm. However, in the absorption spectra based on the periodic model of crystal, there are obvious absorption peaks in the visible region for N-EtPySbBr6, markedly different from the absorption of monomer, implying that N-EtPySbBr₆ is different from other typical 0D perovskite materials with strong quantum confinement. In addition, on the basis of monomer model, we also investigate the polaronic properties of N-EtPySbBr₆. For many molecular crystal³³ and 0D materials,²⁸ small polarons whose radius is less than approximate lattice of unit cell have been observed. Once an electron is added on the monomer, all of the Sb-Br bonds are elongated from 2.59 to 2.74 Å, which preserves the symmetry of octahedral [SbBr₆]⁻¹(see Table S1). From the inset in Figure 3C, it can be seen that the electron spin density is delocalized for all of the monomers, whose contour is similar to that of the sp hybrid orbital. From the absorption spectrum of negative polaronic state, there are rare

absorption in the visible region and a main absorption peak at 270 nm, which can thus be assigned to polaron absorption. When we remove electron from monomer, the symmetry of octahedral is broken. There are two Sb-Br bonds where the spin density distribution is localized on two Br atoms, and the two bonds are elongated from 2.59 to 2.76 Å. Clearly, the two Br atoms are close to each other, while the other four Sb-Br bonds are shortened to 2.50-2.53 Å (see Table S1). The hole spin density is localized on the two Br, which are close to each other (see inset in Figure 3E). The positive polaronic state presents a similar and weak absorption with respect to neutral model (see Figure 3E), implying that polaron absorption is weak. Figure 3D shows the calculated absorption spectrum of dimers. It can be seen that dimer1 and dimer2 have similar absorption spectrum. We also find the absorption peaks are similar to those of monomer except for a slightly strong absorption peak at 400 nm, indicating that interaction among octahedrons may improve absorption in visible region. Figure 3F shows the absorption spectrum of tetramers, where a main absorption peak at 420 nm is seen, confirming that interaction among neighboring octahedrons significantly affects the optoelectronic properties of N-EtPySbBr₆, and can improve the absorption in the visible region.

To characterize the interaction among neighboring octahedrons, we analyze the low-lying dipole allowed singlet excited states of dimer and tetramers by constructing the natural transition orbitals (NTOs). Two hole/particle NTO pairs of dimer and tetramers with a large excitation amplitude are respectively plotted in Figure 4A and B. For dimer, the two excited states correspond to S₁₂ and S₁₉ singlet excited states

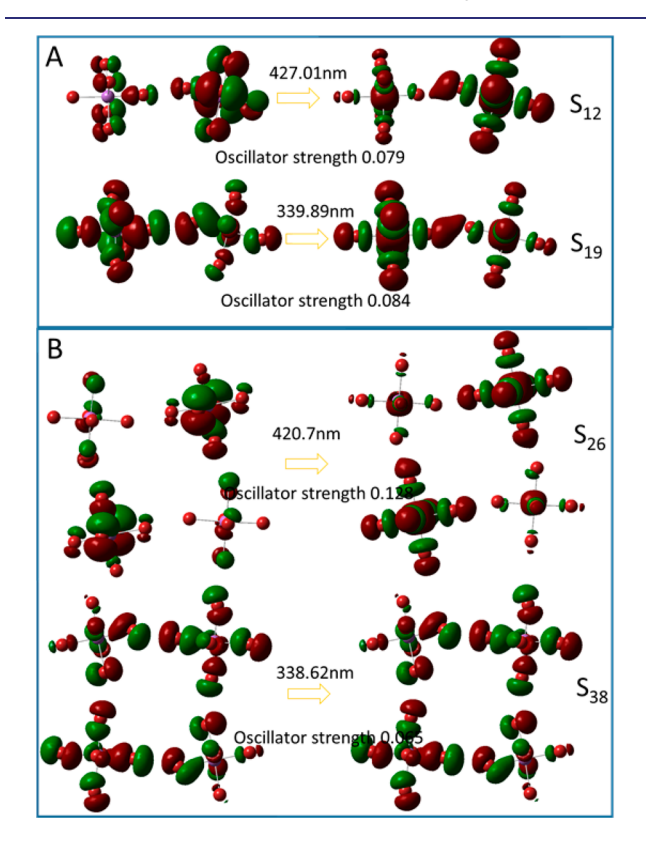


Figure 4. Computed electronic densities of "hole" (right) and "particle" (left) natural transition orbital (NTO) pairs for the dipoleallowed singlet excited states of dimer (A) and tetramers (B) for $[SbBr_6]^{-1}$.

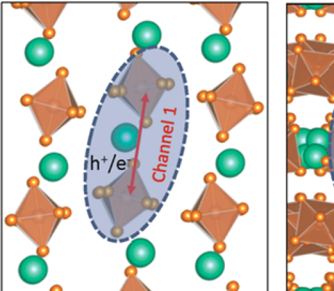
with excitation energies 427.01 and 339.89 nm and corresponding oscillator strengths 0.079 and 0.084, respectively. The photon absorption of dimer arises from the p orbitals \rightarrow sp hybrid orbitals. The electron densities in hole and particle NTOs are delocalized on the two octahedrons, and orbital mixing of the two octahedrons is observed in the two excited states. Once electron is excited, it has a certain probability of transfer to another octahedron, confirming the significant interaction among neighboring octahedrons. Similarly, for tetramers, two hole/particle NTO pairs of S₂₆ and S₃₈ are distributed over all four octahedrons, demonstrating that there is a strong interaction among neighboring octahedrons in N-EtPySbBr₆. Although N-EtPySbBr₆ exhibits the crystal structure of zero dimensionality, its electronic properties are markedly different from those of other typical 0D perovskite materials, in which optoelectronic properties of individual octahedral unit reflect the properties of the crystal due to the weak interaction among neighboring octahedrons.

Analogous to [SbBr₆]⁻¹, [BiCl₆]⁻¹ possesses similar properties because Sb and Bi, Br and Cl, respectively, belong to groups VA and VIIA. Figure S9A-C shows the computed absorption spectra of monomer of [BiCl₆]⁻¹ with different charges. It can be seen that the absorption spectrum of monomer with neutral and positive polaronic state exhibits similar contour. In contrast, there is a clear peak around 320 nm wavelength in the spectrum of monomer with a negative polaronic state, which can be assigned to polaronic absorption. The trend of bond-length change with different charge is also similar to that of [SbBr₆]⁻¹ (see Table S1). From the distributions of spin densities, the negative and positive spin densities are delocalized for monomer, contrary to those of [SbBr₆]. From the spectra of dimer and tetramer, with the increasing size of the octahedron, the absorption peak around 480 nm is significantly improved, demonstrating that the interaction among neighboring octahedrons can also significantly affect the optoelectronic properties of N-EtPyBiCl₆ (see Figure S9D,E). We also calculate the hole/particle NTO pairs of dimer (S_{13}) and tetramers (S_{22}) with a high excitation amplitude (see Figure S10). The electron densities in hole and particle NTOs are delocalized beyond one octahedron, supporting the strong interaction among neighboring octahe-

For N-EtPyVBr₆, we also compute the absorption spectrum of monomer with neutral state, negative polaron state, and positive polaron state, respectively. For neutral state, all of the V-Br bonds are 2.41 Å (see Table S1). As shown in Figure S11A, there are two main absorption peaks at about 620 nm, consistent with calculated absorption spectra of periodic model of crystal. For the negative polaron state, two V-Br bonds are elongated to 2.46 Å and the other four V-Br bonds are elongated to ~2.51 Å (see Table S1), and electron spin densities are localized on the four Br with long V-Br bond length (see the inset in Figure S11B). For the positive polaron state, similar to $[SbBr_6]^{-1}$, two V-Br bonds are elongated to 2.69 Å in which two Br atoms are close to each other, and the hole spin densities are mostly localized on the two Br. Meanwhile, the hole spin densities are slightly delocalized on the V and other two Br in the same plane (see Table S1 and inset in Figure S11C). For the negative polaron state and positive polaron state, there is broad weak absorption between 400 and 550 nm, which may be assigned to polaron absorption (see Figure S11B,C). For dimers and tetramers, there are similar absorption peaks with monomer (see Figure S11D,E), demonstrating that interactions among octahedrons are weak or the interactions do not enhance absorption in visible region. We also calculate the hole/particle NTO pairs of dimer and tetramers with a large excitation amplitude. Figure S12 shows that the hole and particle NTOs are localized on individual octahedron, indicating negligible interaction among neighboring octahedrons. Similar to Cs₄PbBr₆, *N*-EtPyVBr₆ exhibits electronic zero dimensionality with strong quantum confinement.

To our knowledge, vanadium (5+) halide compounds appear to be unstable at room temperature.³⁴ However, halide compounds based on the elements in the same group (Nb and Ta) have been synthesized in a previous study.³⁵ Here, we also investigate N-EtPyNbBr₆ and N-EtPyTaBr₆. Figure S13 shows the computed band structures and DOSs of N-EtPyNbBr₆ and N-EtPyTaBr₆ using the PBE functional. It can be seen that the band structures and contributions of band edges present characters similar to those of N-EtPyVBr₆, except wider bandgaps, whose value is in the order of N-EtPyVBr₆ < N-EtPyNbBr₆ < N-EtPyTaBr₆. Meanwhile, we compute the absorption spectra of monomer, dimer and tetramer of the N-EtPyNbBr₆ (see Figure S14A–E). For monomer with different charges, neutral state possesses the main absorption peak around 390 nm wavelength, while the main absorption peak corresponding to positive and negative polaronic state is slightly blue-shifted to around 350 nm. The negative spin density possesses character of dp hybrid orbital. In contrast, as [VBr₆]⁰, the positive spin density is localized at two Br atoms. From the spectra of dimer and tetramer, with the increasing number of octahedron, the absorption peak around 380 nm is significantly improved. The calculated hole/particle NTO pairs of dimer (S_{31}) and tetramers (S_{54}) with a high excitation amplitude are localized on individual octahedron (see Figure S15) associated with [VBr₆]⁻¹. The optoelectronic features of octahedrons based on group-V transition metal demonstrate a negligible interaction among neighboring octahedrons.

Last, we use the Marcus theory to assess charge carrier mobility of the N-EtPySbBr₆ and N-EtPyBiCl₆, a widely used approach for molecular crystal. From the Marcus theory, two import quantities needed to be estimated, the reorganization energy, $\lambda_{h/e}$, which is the energy cost of charging a single molecule within a molecular crystal, and electronic coupling, $V_{\rm h/e}$, which reflects the strength of the interaction in dimer configuration. For N-EtPySbBr₆, the computed reorganization energies for electron and hole transfer are 1.06 and 1.56 eV, respectively. Clearly, a positive polaronic state breaks the symmetry of the octahedron, which is related to stronger deformations than the negative polaronic state, resulting in higher reorganization energy. The electronic couplings based on the six possible charge hoping channels (see Figure 5) are listed in Table S2. It can be seen that the electronic couplings of electron transfer are significantly larger than those of hole transfer. Because of the lower electron reorganization energy and higher electronic coupling, N-EtPySbBr₆ exhibits a higher intrinsic electron transfer rate, consistent with effective masses. The computed electron mobility is 7.73×10^{-4} cm² V⁻¹ S⁻¹, while the computed hole mobility is 3.67×10^{-7} cm² V⁻¹ S⁻¹. For N-EtPyBiCl6, the computed reorganization energies for electron and hole transfer are 1.03 and 1.59 eV, respectively. The electronic couplings based on the six possible charge hoping channels are listed in Table S3. Similar to N-EtPySbBr₆, the electronic couplings of electron transfer are also larger than those of hole transfer. The computed electron mobility is 5.94



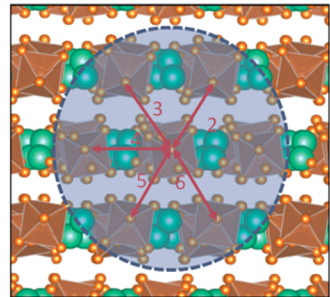


Figure 5. Schematic of charge carrier hopping channel for calculating the charge carrier mobility of *N*-EtPySbBr₆ and *N*-EtPyBiCl₆.

 $\times~10^{-4}~\rm cm^2~V^{-1}~S^{-1}$, while the computed hole mobility is 2.09 $\times~10^{-7}~\rm cm^2~V^{-1}~S^{-1}$. The electron mobility is an order of magnitude higher than the hole mobility, confirming that both N-EtPySbBr₆ and N-EtPyBiCl₆ are n-type semiconductors. The charge carrier mobilities are also significantly higher than those of other 0D materials, for example, electron mobility and hole mobility of Cs₄PbBr₆ (2.2 $\times~10^{-11}$ and 1.4 $\times~10^{-9}~\rm cm^2~V^{-1}~S^{-1}$, respectively). The electron mobility of N-EtPySbBr₆ and N-EtPyBiCl₆ is comparable to that of typical conjugated polymers (e.g., P3HT, $\sim~10^{-4}~\rm cm^2~V^{-1}~S^{-1}$), implying that N-EtPySbBr₆ and N-EtPyBiCl₆ exhibit certain electronic features as a molecular crystal.

In addition, we compute electronic coupling for octahedrons $[VBr_6]^{-1}$, $[NbBr_6]^{-1}$, and $[TaBr_6]^{-1}$. There are weak electronic couplings among neighboring octahedrons for $[VBr_6]^{-1}$, $[NbBr_6]^{-1}$, and $[TaBr_6]^{-1}$ (see Table S4). These weak electronic couplings suggest that $N\text{-EtPyVBr}_6$, $N\text{-EtPyNbBr}_6$, and $N\text{-EtPyTaBr}_6$ possess typical low carrier motilities of 0D perovskites, unsuitable for photovoltaic application. Moreover, for the distributions of the highest occupied molecular orbital (HOMO) and the lowest unoccupied molecular orbitals (LUMO) of dimers for $[SbBr_6]^{-1}$ and $[VBr_6]^{-1}$, they exhibit similar contours of HOMOs (see Figure 6). In contrast, there

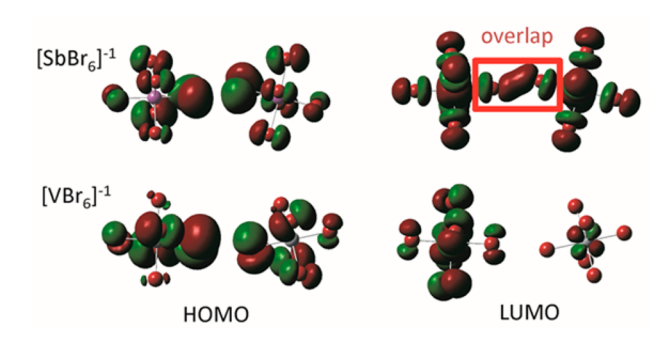


Figure 6. Computed charge density distribution of the HOMO and LUMO for dimers of $\lceil SbBr_6 \rceil^{-1}$ and $\lceil VBr_6 \rceil^{-1}$.

is obvious overlapping among octahedrons of $[SbBr_6]^{-1}$ for LUMO, due to the delocalization of sp hybrid orbital. The LUMO of $[VBr_6]^{-1}$ is mostly localized on one octahedron with little overlapping among the octahedrons due to the localization of the dp hybrid orbital. To seek 0D perovskites with improved optoelectronic properties, we suggest that an effective approach is to examine 0D perovskites with sp hybrid orbitals.

CONCLUSION

We have investigated a series of 0D inorganic/organic lead-free halide perovskite materials using DFT calculations. We find that some compounds based on group VB conduction metals elements (V, Nb, and Ta) exhibit typical features of 0D perovskites, such as low carrier motilities and strong quantum confinement, thereby limiting their applications in optoelectronic devices. Group VA element Sb- and Bi-based 0D perovskites possess features of molecular crystals, such as comparable absorption spectrum of sun light, and carrier mobilities for PV application. The unique properties are due to that the CBM shows a strong hybrid state between the group VA element s orbital and halide p orbital in ASbBr₆ and ABiCl6, and the hybrid states have strong overlap among neighboring octahedrons. Moreover, the bandgap can be tuned over a wide range via tuning the composition in the mixing element strategy. The newly obtained insight into unique optoelectronic property of the 0D perovskites offers a rational design strategy for low-dimensional perovskites to address some known challenging issues inherent in the lead halide perovskite solar cells.

COMPUTATIONAL METHODS

The first-principles computations for periodic systems are performed on the basis of density-functional theory (DFT) methods as implemented in the Vienna ab initio simulation package (VASP 5.4).36 An energy cutoff of 520 eV is employed, and the atomic positions are optimized using the conjugate gradient scheme without any symmetric restrictions until the maximum force on each atom is less than 0.02 eV Å-1. The ion cores are described by using the projector augmented wave (PAW) method.³⁷ Grimme's DFT-D3 correction is adopted to describe the long-range van der Waals interaction.³⁸ A $2 \times 6 \times 2$ k-point grid is used for the ABX₆. The electronic structures and the optical properties are computed by using HSE06 functional with a cutoff energy of 400 eV.39 The two parameters in the HSE06 functional, α and ω , control respectively the mixing and screening of the Hartree–Fock exchange. Here, we fix α at 0.25 following an argument based on the adiabatic connection formula, while uses a smaller ω (0.1 Å⁻¹) than the standard value (0.2 ${
m \AA}^{-1}$). With the modified ω , our HSE06 calculation yields a band gap of 1.55 eV for N-EtPySbBr₆, in good agreement with the experiment.³⁰ The bandgaps of a series of ASbBr₆ compounds are computed on the basis of the HSE06 functional with only the Γ point. To reduce the computational cost of electronic structures for N-EtPySbBr₆, N-EtPyBiCl₆, and N-EtPyVBr₆, we replace N-EtPy⁺ with Cs⁺ and freeze the lattices and other atoms. Because the N-EtPy⁺ does not contribute to the bandgap edge, the band structure and DOS around the bandgap edge are not affected. The absorption coefficient is given by $\frac{\sqrt{2}\,\epsilon}{\hbar c}[(\varepsilon_1^{\ 2}+\varepsilon_2^{\ 2})^{1/2}-\varepsilon_1]^{1/2}\frac{\sqrt{2}\,\epsilon}{\hbar c}[(\varepsilon_1^{\ 2}+\varepsilon_2^{\ 2})^{1/2}-\varepsilon_1]^{1/2},$ where ε_1 and ε_2 are the real and imaginary parts of the dielectric function, respectively.

For the monomers of $[BX_6]^{-1}$, the neutral and charged geometries are optimized with the B3LYP hybrid functional implanted in Gaussian 09 code. V, Nb, Ta, Bi, and Sb are described using the LANL2DZ basis set, and Br and Cl are described using the 6-31G** basis set. On the basis of monomers, dimers, and tetramers, in which configurations of dimers and tetramers in crystal are adopted without optimization for preserving the relative configures among the octahedrons, hybrid long-range corrected functional @B97XD⁴⁰ used to compute the optical absorption spectrum using the TDDFT

The charge transfer rates between neighboring octahedrons are described by the Marcus theory ⁴¹ following the equation $k_{\text{h/e}} = \frac{4\pi^2}{h} \frac{1}{\sqrt{4\pi \lambda_{\text{h/e}} k_{\text{B}} T}} V_{\text{h/e}}^2 \exp\left(-\frac{\lambda_{\text{h/e}}}{4k_{\text{B}} T}\right)$, where T is temperature, k_{B} is Boltzmann constant, h is Planck constant, $\lambda_{\text{h/e}}$ is the hole or electron reorganization energy, and $V_{\rm h/e}$ refers to the electronic coupling, calculated by using the NWCHEM code. ⁴² The formula used for this calculation is $V_{\rm AB}=\frac{|H_{\rm A}-S_{\rm AB}(H_{\rm AA}+H_{\rm BB})~/~2|}{1-S_{\rm AB}^2}$, with $H_{\rm AB}=\langle\psi_{\rm A}|H|~\psi_{\rm B}\rangle$ and $S_{AB}(\psi_A|\psi_B)^{43}$ These calculations are performed at the unrestricted Hartree–Fock level with the 6-311G** basis set for Br and Cl and the LANL2DZ basis set for Sb, Bi, V, Nb and Ta. The hole or electron motility is estimated by the Einstein relation $\mu = \frac{eD}{k_{\mathrm{B}}T}$, where e is the electron charge and D is the charge diffusion coefficient, which can be evaluated from $D = \frac{1}{2n} \sum_i d_i^2 k_i P_i$, where n is the spatial dimension, k_i is the charge transfer rate along each direction, d_i is the corresponding

ASSOCIATED CONTENT

S Supporting Information

The Supporting Information is available free of charge on the ACS Publications website at DOI: 10.1021/jacs.8b03917.

hopping distance, and P_i is the relative probability, given by $P_i = \frac{k_i}{\sum k_i}$.

Additional calculation and analysis data shown in Figures S1-S15 and Tables S1-S4 (PDF)

AUTHOR INFORMATION

Corresponding Author

*xzeng1@unl.edu

ORCID

Ming-Gang Ju: 0000-0003-4285-7937

Jun Dai: 0000-0001-6599-8826 Liang Ma: 0000-0003-4747-613X

Xiao Cheng Zeng: 0000-0003-4672-8585

The authors declare no competing financial interest.

ACKNOWLEDGMENTS

X.C.Z. was supported by the National Science Foundation (NSF) through the Nebraska Materials Research Science and Engineering Center (MRSEC) (grant no. DMR-1420645), an NSF EPSCoR Track 2 grant (OIA-1538893), and by the University of Nebraska Holland Computing Center. Y.Z. acknowledges the support from the National Science Foundation (OIA-1538893), the Office for Naval Research (N00014-17-1-2232), and the support from Prof. Nitin P. Padture at Brown University.

REFERENCES

- (1) Eperon, G. E.; Leijtens, T.; Bush, K. A.; Prasanna, R.; Green, T.; Wang, J. T.-W.; McMeekin, D. P.; Volonakis, G.; Milot, R. L.; May, R. Science 2016, 354, 861.
- (2) Zong, Y.; Wang, N.; Zhang, L.; Ju, M.-G.; Zeng, X. C.; Sun, X. W.; Zhou, Y.; Padture, N. P. Angew. Chem., Int. Ed. 2017, 56, 12658.
- (3) Yablonovitch, E. Science 2016, 351, 1401.
- (4) Stranks, S. D.; Snaith, H. J. Nat. Nanotechnol. 2015, 10, 391.
- (5) Green, M. A.; Ho-Baillie, A.; Snaith, H. J. Nat. Photonics 2014, 8,
- (6) Kojima, A.; Teshima, K.; Shirai, Y.; Miyasaka, T. J. Am. Chem. Soc. 2009, 131, 6050.
- (7) Park, B. W.; Philippe, B.; Zhang, X.; Rensmo, H.; Boschloo, G.; Johansson, E. M. J. Adv. Mater. 2015, 27, 6806.
- (8) Bekenstein, Y.; Koscher, B. A.; Eaton, S. W.; Yang, P.; Alivisatos, A. P. J. Am. Chem. Soc. 2015, 137, 16008.
- (9) Ramasamy, P.; Lim, D.-H.; Kim, B.; Lee, S.-H.; Lee, M.-S.; Lee, J.-S. Chem. Commun. 2016, 52, 2067.
- (10) https://www.nrel.gov/pv/assets/images/efficiency-chart-20180716.jpg.

- (11) Marshall, K. P.; Walker, M.; Walton, R. I.; Hatton, R. A. Nat. Energy 2016, 1, 16178.
- (12) Ju, M.-G.; Dai, J.; Ma, L.; Zeng, X. C. Adv. Energy Mater. 2017, 1700216.
- (13) Wang, N.; Zhou, Y.; Ju, M. G.; Garces, H. F.; Ding, T.; Pang, S.; Zeng, X. C.; Padture, N. P.; Sun, X. W. Adv. Energy Mater. **2016**, *6*, 1601130.
- (14) Ju, M.-G.; Dai, J.; Ma, L.; Zeng, X. C. J. Am. Chem. Soc. 2017, 139, 8038.
- (15) Stoumpos, C. C.; Frazer, L.; Clark, D. J.; Kim, Y. S.; Rhim, S. H.; Freeman, A. J.; Ketterson, J. B.; Jang, J. I.; Kanatzidis, M. G. *J. Am. Chem. Soc.* **2015**, *137*, 6804.
- (16) Saparov, B.; Hong, F.; Sun, J.-P.; Duan, H.-S.; Meng, W.; Cameron, S.; Hill, I. G.; Yan, Y.; Mitzi, D. B. Chem. Mater. 2015, 27, 5622.
- (17) Greul, E.; Petrus, M. L.; Binek, A.; Docampo, P.; Bein, T. J. Mater. Chem. A 2017, 5, 19972.
- (18) Slavney, A. H.; Hu, T.; Lindenberg, A. M.; Karunadasa, H. I. J. Am. Chem. Soc. **2016**, 138, 2138.
- (19) Giustino, F.; Snaith, H. J. ACS Energy Lett. 2016, 1, 1233.
- (20) Ju, M.-G.; Chen, M.; Zhou, Y.; Garces, H. F.; Dai, J.; Ma, L.; Padture, N. P.; Zeng, X. C. *Joule* **2018**, *2*, 1231–1241.
- (21) Lin, H.; Zhou, C.; Tian, Y.; Siegrist, T.; Ma, B. ACS Energy Lett. **2018**. 3, 54.
- (22) Tsai, H.; Nie, W.; Blancon, J.-C.; Stoumpos, C. C.; Asadpour, R.; Harutyunyan, B.; Neukirch, A. J.; Verduzco, R.; Crochet, J. J.; Tretiak, S. *Nature* **2016**, *536*, 312.
- (23) Ma, L.; Dai, J.; Zeng, X. C. Adv. Energy Mater. 2017, 7, 1601731.
- (24) Wang, S.; Mitzi, D. B.; Feild, C. A.; Guloy, A. J. Am. Chem. Soc. 1995, 117, 5297.
- (25) Yuan, Z.; Zhou, C.; Tian, Y.; Shu, Y.; Messier, J.; Wang, J. C.; Van De Burgt, L. J.; Kountouriotis, K.; Xin, Y.; Holt, E. *Nat. Commun.* **2017**, *8*, 14051.
- (26) Saidaminov, M. I.; Mohammed, O. F.; Bakr, O. M. ACS Energy Lett. 2017, 2, 889.
- (27) Mitzi, D. B.; Liang, K.; Wang, S. Inorg. Chem. 1998, 37, 321.
- (28) Yin, J.; Maity, P.; De Bastiani, M.; Dursun, I.; Bakr, O. M.; Brédas, J.-L.; Mohammed, O. F. Sci. Adv. 2017, 3, e1701793.
- (29) Ju, M.-G.; Chen, M.; Zhou, Y.; Garces, H. F.; Dai, J.; Ma, L.; Padture, N. P.; Zeng, X. C. ACS Energy Lett. 2018, 3, 297.
- (30) Adonin, S. A.; Frolova, L. A.; Sokolov, M. N.; Shilov, G. V.; Korchagin, D. V.; Fedin, V. P.; Aldoshin, S. M.; Stevenson, K. J.; Troshin, P. A. *Adv. Energy Mater.* **2018**, *8*, 1701140.
- (31) Chen, M.; Ju, M.-G.; Carl, A. D.; Zong, Y.; Grimm, R. L.; Gu, J.; Zeng, X. C.; Zhou, Y.; Padture, N. P. Joule 2018, 2, 558.
- (32) Maughan, A. E.; Kurzman, J. A.; Neilson, J. R. Inorg. Chem. 2015, 54, 370.
- (33) Zaikowski, L.; Kaur, P.; Gelfond, C.; Selvaggio, E.; Asaoka, S.; Wu, Q.; Chen, H.-C.; Takeda, N.; Cook, A. R.; Yang, A. *J. Am. Chem. Soc.* **2012**, *134*, 10852.
- (34) Tamadon, F.; Seppelt, K. Angew. Chem., Int. Ed. 2013, 52, 767.
- (35) Van Bronswyk, W.; Clark, R. J. H.; Maresca, L. Inorg. Chem. 1969, 8, 1395.
- (36) Kresse, G.; Furthmüller, J. Comput. Mater. Sci. 1996, 6, 15.
- (37) Kresse, G.; Joubert, D. Phys. Rev. B: Condens. Matter Mater. Phys. 1999, 59, 1758.
- (38) Grimme, S.; Antony, J.; Ehrlich, S.; Krieg, H. J. Chem. Phys. 2010, 132, 154104.
- (39) Heyd, J.; Scuseria, G. E.; Ernzerhof, M. J. Chem. Phys. 2003, 118, 8207.
- (40) Chai, J.-D.; Head-Gordon, M. J. Chem. Phys. 2008, 128, 084106.
- (41) Marcus, R. A. Rev. Mod. Phys. 1993, 65, 599.
- (42) Kendall, R. A.; Aprà, E.; Bernholdt, D. E.; Bylaska, E. J.; Dupuis, M.; Fann, G. I.; Harrison, R. J.; Ju, J.; Nichols, J. A.; Nieplocha, J. Comput. Phys. Commun. 2000, 128, 260.
- (43) Farazdel, A.; Dupuis, M.; Clementi, E.; Aviram, A. J. Am. Chem. Soc. 1990, 112, 4206.